THE ASTROPHYSICAL JOURNAL, 1000:203 (10pp), 2026 April 1 https://doi.org/10.3847/1538-4357/ae4c40

Evolution of a Pickup Ion Ring-beam Population in Large-scale Interstellar Turbulence and Small-scale Self-generated Waves: Implications for the IBEX Ribbon

Yifan Huang[1], Fan Guo[2], Xiaochen Sun[3], Sung Jun Noh[2], Eric J. Zirnstein[3], Daniel B. Reisenfeld[2], Hui Li[2], Vladimir Florinski[1,4], and Jacob Heerikhuisen[5]

[1] Center for Space Plasma and Aeronomic Research, University of Alabama in Huntsville, Huntsville, AL, USA; yh0017@uah.edu
[2] Los Alamos National Laboratory, Los Alamos, NM, USA
[3] Department of Astrophysical Sciences, Princeton University, Princeton, NJ, USA
[4] Department of Space Science, University of Alabama in Huntsville, Huntsville, AL, USA
[5] University of Waikato, Hillcrest, Hamilton, New Zealand

Received 2026 January 24; revised 2026 February 21; accepted 2026 February 27; published 2026 March 24

Abstract

The secondary energetic neutral atom (ENA) mechanism proposed to explain the ribbon-like enhancement of ENA emission observed by Interplanetary Boundary Explorer (IBEX) involves a pickup ion (PUI) ring-beam population beyond the heliopause. The stability of this highly anisotropic PUI distribution is crucial for determining the physical process responsible for the ribbon formation. It has been proposed that PUIs with pitch angles near 90° can become trapped via the magnetic mirroring process in the turbulent magnetic field of the local interstellar medium. However, the turbulent mirroring scenario typically neglects self-generated waves excited by the kinetic instabilities of the ring-beam PUIs, which can efficiently scatter PUIs in pitch angle. Using a magnetohydrodynamics–particle-in-cell approach implemented in ATHENA++, we simulate the evolution of the ring-beam PUIs, incorporating both large-scale interstellar magnetic fluctuations and microscale self-excited instabilities. We examine the competition between turbulent mirroring and pitch-angle scattering by the self-generated waves. Our results show that the PUIs can be rapidly scattered toward a nearly isotropic distribution on the order of one day, much shorter than their characteristic lifetime of a couple of years. This suggests that theoretical difficulties remain for maintaining an anisotropic PUI distribution in physical models of the IBEX ribbon.

Unified Astronomy Thesaurus concepts: Pickup ions (1239); Heliosphere (711); Magnetohydrodynamics (1964); Space plasmas (1544); Interstellar medium (847); Interstellar magnetic fields (845); Particle physics (2088)

1. Introduction

The Interplanetary Boundary Explorer (IBEX; D. J. McComas et al. 2009a) observed a narrow band of enhanced energetic neutral atom (ENA) emission with energy ∼500 eV to ∼6 keV across the sky via its IBEX-Hi instrument (H. O. Funsten et al. 2009a), known as the IBEX ribbon. The ENA emission has an intensity ∼3 times brighter than the surrounding globally distributed flux and varies in width, with a full width at half-maximum ranging from ∼15° to ∼25°, depending on the energy channel (H. O. Funsten et al. 2009b; S. A. Fuselier et al. 2009; D. J. McComas et al. 2009b, 2010; S. J. Noh et al. 2025; D. B. Reisenfeld et al. 2026). It is widely believed that the ENAs of the IBEX ribbon are coming from the region outside the heliopause where the line of sight ($\boldsymbol{r}$) is approximately normal to the local interstellar magnetic field (LISMF; N. V. Pogorelov et al. 2009; N. A. Schwadron et al. 2009), i.e., $\boldsymbol{B} \cdot \boldsymbol{r} \sim 0$. Numerous theories and models have been developed to explore the origin of the ribbon (see D. J. McComas et al. 2014, and references therein, as well as more recent models such as P. A. Isenberg 2014, J. Giacalone & J. R. Jokipii 2015, E. J. Zirnstein et al. 2020, and S. Xu & H. Li 2023). The most accepted explanation for this origin is the so-called secondary ENA mechanism (D. J. McComas et al. 2009b). As the solar wind (SW) flows radially away from the Sun, typically at speeds ranging from about 300–800 km s^{-1}, a population of the SW ions becomes neutralized due to charge exchange with interstellar neutrals, and the resulting atoms continue to propagate with the velocities of the parent SW ions. The neutralized SW (NSW) particles, also known as primary ENAs, propagate outward through the heliosphere with mean free paths that can reach thousands of astronomical units (au); after entering the VLISM, their mean free paths decrease to hundreds of au or less, and charge exchange with interstellar thermal ions converts them into pickup ions (PUIs). With a mean lifetime of $\sim 1-2$ yr, those PUIs undergo another charge exchange with the interstellar neutrals and become secondary ENAs, some of which may propagate back to the inner heliosphere and be detected by the IBEX as ribbon ENAs.

The secondary ENA concept can be manifested via two distinct scenarios. One is known as the "weakly scattering" scenario, in which the ring-beam PUIs maintain an anisotropic velocity distribution that is preferentially perpendicular to the LISMF. The numerical simulations based on this scenario could reproduce a comparable ENA intensity with IBEX observations (e.g., J. Heerikhuisen et al. 2010; E. J. Zirnstein et al. 2018; Y. Huang et al. 2025). However, V. Florinski et al. (2010) noted that such a ring-beam distribution would excite magnetic fluctuations and thereby isotropize PUIs on a timescale much shorter than the lifetime of the PUIs. Some subsequent studies indicate that rapid isotropization may not be inevitable. For example, the Alfvén–ion-cyclotron (AIC) wave growth rate depends on the ring's perpendicular thermal spread (i.e., ring thickness) and local plasma conditions, and there exists a "stability gap" in which broadened rings have a strongly reduced growth rate and can persist much longer (E. J. Summerlin et al. 2014; V. Florinski et al. 2016). Complementary kinetic studies further suggest that stability can occur when the distribution is neither too narrow nor too broad; however, adding an additional, broader PUI component (hot "halo" PUIs) can restore stronger wave growth and accelerate isotropization (J. Niemiec et al. 2016). Thus, the stability of ring-beam PUIs remains an active topic, with many studies still reaching opposite conclusions under different conditions (e.g., K. V. Gamayunov et al. 2017, 2019; K. Min & K. Liu 2018; A. Mousavi et al. 2020, 2022, 2025). To avoid relying on sustained weak scattering, N. A. Schwadron & D. J. McComas (2013) proposed a "spatial retention" scenario, in which the PUIs could be trapped due to the resonance of PUIs with the generated Alfvén waves. Based on the spatial retention model, the ribbon simulation by E. J. Zirnstein et al. (2019) shows that the simulated ENA intensity of the ribbon is approximately 2 times smaller than in the observation, indicating that an additional source of enhanced PUIs is needed.

J. Giacalone & J. R. Jokipii (2015) proposed a new model for the IBEX ribbon, suggesting that the magnetic turbulence can efficiently trap ions with initial pitch angles near 90° through mirroring effects (see also E. J. Zirnstein et al. 2020; S. Xu & H. Li 2023; E. J. Zirnstein et al. 2025). In their test particle simulation, the velocity distribution of PUIs within the ribbon's ENA production region (where $\boldsymbol{B} \cdot \boldsymbol{r} \sim 0$) is strongly anisotropic, exhibiting a pronounced peak near 90°. In the regions with lines of sight approximately $10^\circ - 15^\circ$ from the $\boldsymbol{B} \cdot \boldsymbol{r} \sim 0$ direction, a group of reflected particles in the velocity distribution is seen, revealing the mirroring process. However, the turbulent mirroring model neglects the magnetic fluctuations excited by the microscale instabilities of the PUI ring beam, which may efficiently scatter the PUIs. Therefore, it remains unclear whether turbulent mirroring can dominate over PUI scattering by self-generated waves in maintaining an anisotropic PUI distribution.

To investigate this problem, in this paper, we simulate the evolution of the ring-beam PUIs in both large-scale interstellar magnetic fluctuation and microscale self-generated waves, using a magnetohydrodynamics–particle-in-cell (MHD–PIC) approach implemented in ATHENA++ (X. Sun & X.-N. Bai 2023). In this method, the background plasma is treated as an MHD fluid. The PUIs ionized from the neutral SW are treated as macroparticles, which are collisionless on the timescale of interest, so that they are only subject to the Lorentz force. The PUIs provide feedback to the background plasma through their bulk quantities, such as charge density and current density (X.-N. Bai et al. 2015), similar to the traditional PIC/hybrid–PIC approach (V. Florinski et al. 2010; V. Roytershteyn et al. 2019). In our 1D simulation, the PUIs have an initial ring-beam-like distribution, and the magnetic fluctuations of interstellar turbulence are initialized as Alfvén waves whose power spectrum matches the observations by Voyager 1. Even though the large-scale magnetic fluctuations restrict the PUI pitch-angle scattering through mirroring effects, our simulation results show that the PUIs generate Alfvén-ion-cyclotron waves and are scattered to a nearly isotropic distribution due to the self-generated waves within a short duration (∼several days) compared to their lifetime of a few years. Therefore, theoretical difficulties remain for maintaining an anisotropic PUI distribution in physical models of the IBEX ribbon.

The paper is organized as follows: in Section 2, we introduce the methodology of the MHD–PIC simulations, including the governing equations (Section 2.1), the setup of background plasma and particles (Section 2.2), and initialization of preexisting magnetic fluctuations (Section 2.3). We discuss the evolution of the magnetic fluctuation and PUI distribution in Section 3. A summary and a discussion are provided in Section 4.

2. Methodology

ATHENA++ is a high-performance, state-of-the-art framework for MHD simulations in plasma physics (J. M. Stone et al. 2020). In this work, we employ the hybrid MHD–PIC module, recently integrated into ATHENA++, for modeling the kinetic behavior of energetic particles (X. Sun & X.-N. Bai 2023). In this method, only the energetic particle population (e.g., pickup ions or cosmic rays) is represented by macroparticles, whereas the rest of the plasma is treated as a continuum fluid governed by the MHD equations. The macroparticles experience only the Lorentz force, and their feedback on the MHD fluid is incorporated through their number and current densities. In our problem, the particle population is initialized with a prescribed velocity distribution (ring beam introduced in Section 2.2), which includes a finite velocity-space spread as appropriate for the application.

This MHD–PIC method has previously been applied to investigate magnetic fluctuations driven by energetic particles and the associated evolution of their pitch-angle distributions (e.g., X.-N. Bai et al. 2019). Here, we apply the MHD–PIC code to simulate the evolution of the ring-beam PUI population in the presence of both externally imposed large-scale magnetic fluctuations and self-generated waves. We also perform a comparison run in which the PUI feedback to the MHD fluid is disabled. This allows us to investigate the impact of self-generated waves on PUI evolution, in addition to the effects of turbulent magnetic mirroring.

2.1. The Governing Equations

Since in our work the PUIs have energies of ~ 1 keV, their governing equations are nonrelativistic:

$$\frac{d\boldsymbol{x}}{dt} = \boldsymbol{v}, \tag{1}$$

$$\frac{d\boldsymbol{v}}{dt} = \frac{q}{m}\left(\boldsymbol{E} + \frac{1}{c}\boldsymbol{v} \times \boldsymbol{B}\right), \tag{2}$$

where $\boldsymbol{x}$, $\boldsymbol{v}$, q, m, and c are the position, velocity, charge, mass of the particle, and the speed of light, respectively, while $\boldsymbol{E}$ and $\boldsymbol{B}$ are the electric and magnetic fields at the particle positions, respectively.

In this model, we expect the PUI density to be much smaller than the plasma density, i.e., $N_{\rm PUI} \ll N_i \simeq N_e$, and this is the regime where the formulation can be applicable. The MHD equations of the plasma fluid, including the feedback from the PUIs, are (X.-N. Bai et al. 2015)

$$\partial_t \rho + \nabla \cdot (\rho \boldsymbol{u}) = 0, \tag{3}$$

$$\partial_t(\rho \boldsymbol{u}) + \nabla \cdot (\rho \boldsymbol{u}\boldsymbol{u} - \boldsymbol{B}\boldsymbol{B}) + \nabla(P + B^2/2) = -(qN_{\rm PUI}\boldsymbol{E} + \frac{1}{c}\boldsymbol{J}_{\rm PUI} \times \boldsymbol{B}), \quad (4)$$

$$\partial_t\mathcal{E} + \nabla \cdot [(\mathcal{E} + P + B^2/2)\boldsymbol{u} - (\boldsymbol{u} \cdot \boldsymbol{B})\boldsymbol{B}] = -\boldsymbol{J}_{\rm PUI} \cdot \boldsymbol{E}, \quad (5)$$

where ρ is fluid density, $\boldsymbol{u}$ is bulk velocity, P is pressure, and the fluid energy density $\mathcal{E}$ is given by

$$\mathcal{E} = \frac{P}{\Gamma - 1} + \frac{1}{2}\rho u^2 + \frac{1}{2}B^2, \quad (6)$$

where $\Gamma = 5/3$ is the adiabatic index. Note that the unit for magnetic field has magnetic permeability being one, and factors of $1/\sqrt{4\pi}$ are absorbed. In each cell, the PUI number density $N_{\rm PUI}$ and current density $\boldsymbol{J}_{\rm PUI}$ are given by

$$N_{\rm PUI} \equiv \int f(t, \boldsymbol{x}, \boldsymbol{v}) d^3\boldsymbol{v}, \quad (7)$$

$$\boldsymbol{J}_{\rm PUI} \equiv q\int \boldsymbol{v} f(t, \boldsymbol{x}, \boldsymbol{v}) d^3\boldsymbol{v} = qN_{\rm PUI}\boldsymbol{U}_{\rm PUI}, \quad (8)$$

where $f(t, \boldsymbol{x}, \boldsymbol{v})$ is the phase distribution function of PUIs, and $\boldsymbol{U}_{\rm PUI}$ is the mean drift velocity of the PUIs.

In the MHD–PIC method, the induction equation is

$$\partial_t\boldsymbol{B} = -\nabla \times (c\boldsymbol{E}), \quad (9)$$

and the generalized Ohm's law in the presence of PUIs can be written as

$$\boldsymbol{E} = -\frac{\boldsymbol{u}}{c} \times \boldsymbol{B} - R\,\frac{(\boldsymbol{U}_{\rm PUI} - \boldsymbol{u})}{c} \times \boldsymbol{B}, \quad (10)$$

where $R \equiv N_{\rm PUI}/N_{\rm total}$ is the ratio of the PUI number density to the total number density.

In Equation (10), the first term on the right-hand side is the conventional inductive term in MHD, and the second term is an additional contribution arising from the presence of PUIs (hereafter the PUI–Hall term). We have neglected the conventional Hall term, $\propto \boldsymbol{J} \times \boldsymbol{B}$, and the electron pressure gradient term, $\propto \nabla P_e$, which become important at scales comparable to or smaller than the ion inertial length, i.e., $kd_i \gtrsim 1$ (k is the wavenumber, d_i is the ion inertial length, $d_i \equiv c/\omega_{pi}$, and ω_{pi} is the ion plasma frequency). In our setup, the resonant wavelength at initialization is $\lambda_{\rm res0} = 2\pi v_{\|0}/\Omega_i \simeq 2\pi d_i$ with $v_{\|0} \simeq V_{\rm A}$ (Section 2.2), but the waves that carry the largest power excited by the ring-beam PUIs occur at much larger scales, $\sim 2\pi v_{\perp 0}/\Omega_i \simeq 16\,\lambda_{\rm res0}$. Therefore, for the dominant wave power in our simulations, $kd_i \ll 1$, and it is justified to neglect the conventional Hall and ∇P_e terms.

Furthermore, following X.-N. Bai et al. (2015), we quantify the importance of the PUI–Hall term using

$$\Lambda \equiv \frac{R(U_{\rm PUI} - u)}{V_{\rm A}}, \quad (11)$$

which measures the PUI-induced electron–ion drift, $R(U_{\rm PUI} - u)$, in units of the Alfvén speed. The PUI–Hall term significantly modifies the magnetic-field induction only when this drift becomes Alfvénic ($\Lambda \sim 1$). In our simulations, as $R \ll 1$, we observe $\Lambda \ll 1$, which confirms that the PUI–Hall term has a negligible effect on the results.

In the MHD–PIC code, we solve the MHD equations using the van Leer integrator (B. van Leer 1979) with piecewise parabolic reconstruction and the Roe Riemann solver (J. M. Stone & T. Gardiner 2009; J. M. Stone et al. 2020), and we advance the kinetic particles with the Boris pusher (J. Boris et al. 1971). To integrate for a full time step Δt, the van Leer time integrator and the Boris pusher employ two stages with midpoint states of the physical quantities at $t^{\rm mid} = t^{\rm ini} + \Delta t/2$ so that they can achieve second-order temporal accuracy. The integration time step Δt is adaptive. In the van Leer integrator, Δt is constrained to satisfy the standard Courant–Friedrichs–Lewy stability condition (J. M. Stone & T. Gardiner 2009). In the Boris pusher, during a time step Δt, we ensure that particles cannot cross more than two cells or rotate by more than 0.3 radians, a condition that has been tested to ensure sufficient accuracy in particle orbital integration. See X. Sun & X.-N. Bai (2023) for more details on the implementation.

2.2. Setups for Background Plasma and PUI Particles

In this paper, we are interested in the pitch-angle distribution of PUIs in the ribbon ENA source region, where the line of sight is nearly perpendicular to the LISM. For simplicity, we neglect the draping geometry of the LISMF and set up a 1D simulation box that is aligned along the ambient magnetic field $B = B_0\hat{x}$ with periodic boundaries. In the simulation box, we assume a homogeneous magnetized plasma with the ambient magnetic field $B_0 = 4\,\mu$G, plasma density $n_0 = 0.1$ cm^{-3}, and temperature $T = 2 \times 10^4$ K (J. Heerikhuisen et al. 2016; E. J. Zirnstein et al. 2020). These parameters correspond to the sound speed $c_s \simeq 16.6$ km s^{-1}, Alfvén speed $V_{\rm A} \simeq 27.6$ km s^{-1}, ion cyclotron frequency $\Omega_i \simeq 0.038$ s^{-1}, and ion inertial length $d_i \simeq 725$ km. The cell length is $\Delta_x = 0.5\,d_i$ and the total box size is $L_x = 5.12 \times 10^6\Delta_x$, which corresponds to about 12.4 au. The reason to choose this box size is that the scale of the magnetic fluctuations outside the heliopause is estimated to be tens of au (E. J. Zirnstein et al. 2020).

To initialize the PUIs with a ring-beam distribution, we refer to a fitted parent NSW velocity distribution from the global heliosphere model in J. Heerikhuisen et al. (2016). We choose the parent NSW velocity distribution at $r = 136$ au in the direction toward the ecliptic J2000 coordinates (258°.63, −21°.78), shown in their Figure 8. In the phase space distribution $f(v_\perp, v_\|)$, the ring-beam distribution appears as a thin, elongated ridge, in which the phase-space density is concentrated over a broad range of $v_\perp$ (the "ring"), while $v_\|$ is narrowly distributed with a small net drift (the "beam"). For simplicity, we ignore the dependence of the ionization rate on the speed of NSW particles as it makes little difference in the densest region in the distribution for PUIs, which contributes the most to the excited waves. Under this approximation, the parent NSW distribution provides the relative phase-space density of PUIs, so we construct the normalized PUI distribution by setting $f_{\rm PUI}(\boldsymbol{v}) \propto f_{\rm NSW}(\boldsymbol{v})$ and determining the proportionality constant from $\int f_{\rm PUI}\,d^3v = N_{\rm PUI}$. In our problem, we set the absolute normalization by adopting a PUI number density of $N_{\rm PUI} = 10^{-4}\,n_0$, consistent with the values extracted from the global heliosphere models used in J. Heerikhuisen et al. (2016) and E. J. Zirnstein et al. (2016).

In our MHD–PIC simulations, the number of particles per cell (nppc) is set to 100. Unlike the traditional hybrid–PIC/PIC simulation, the MHD–PIC code has significantly reduced the numerical noise as the background plasma is treated as a fluid. Test runs with nppc values ranging from 10^2 to 10^4 show negligible differences in the evolution of self-generated waves and pitch-angle scattering of the ring-beam PUIs. These results confirm that the numerical noise in our simulation is much weaker than the magnetic fluctuations physically excited by PUI ring-beam instabilities. Therefore, we adopt nppc = 100 in this work, which is sufficient to capture key physical processes.

2.3. The Preexisting Magnetic Fluctuations of Interstellar Turbulence

Observations from Voyager 1 and Voyager 2 beyond the heliopause have demonstrated that the local interstellar medium exhibits broadband magnetic field fluctuations (L. F. Burlaga et al. 2015, 2018). These observations indicate that turbulence persists outside the heliopause and plays a critical role in the energetic particle dynamics. G. P. Zank et al. (2019) suggested that compressible turbulence near the heliopause soon experiences mode conversion to incompressible turbulence in the low-beta VLISM plasma. We approximate the local interstellar magnetic field fluctuations as a slab spectrum of parallel propagating Alfvénic fluctuations (e.g., J. R. Jokipii 1966; R. Schlickeiser 2002). While this treatment omits the multi-directional dynamics present in fully 3D turbulence, our simulation does include an inhomogeneous distribution of magnetic field magnitude and thus can support the mirroring effect (see simulation results for details). In the future, it will be useful to investigate whether more realistic turbulence models alter any of the conclusions.

In our 1D simulation, we initialize the system with a spectrum of Alfvén waves propagating along the ambient magnetic field. The wave power at any given wavenumber follows the Kolmogorov spectrum in a normalized form (L. F. Burlaga et al. 2018; J. Giacalone & J. R. Jokipii 1999; E. J. Zirnstein et al. 2020):

$$P(k) = \frac{5\sin(3\pi/5)}{3\pi}\frac{\sigma^2 L_C}{1 + (kL_C)^{5/3}}, \tag{12}$$

in which σ^2 is the wave variance, and L_C is the correlation length. The broadband fluctuation is represented by a range of discretized wavenumbers:

$$k_n = n\frac{2\pi}{N_c\Delta_x},\ 1 \leqslant n \leqslant N_c/2, \tag{13}$$

where N_c is the number of cells in the simulation box and Δ_x is the cell length. For each k_n, we initiate four modes with the same amplitude corresponding to forward and backward propagation and left and right polarization with random phase. Therefore, for different k_n, the wave amplitude $A_n(k_n)$ of each mode is

$$A_n^2(k_n) = \frac{P(k_n)\Delta k_n}{4}, \tag{14}$$

where Δk_n is the wavenumber interval $\Delta k_n = 2\pi/(N_c\Delta_x)$. For our simulation with total box size of $L_x = 2.56 \times 10^6\, d_i$ and cell size $\Delta_x = 0.5\, d_i$, the rms strength of magnetic fluctuations is about $0.352\,\mu G$, i.e., $\delta B/B_0 \simeq 0.088$.

3. Simulation Results

In this section, we examine and compare the pitch-angle evolution of PUIs under two distinct cases. In the first case, we exclude the self-generated waves from ring-beam instabilities by disabling the PUI feedback on the background MHD fluid (test-particle limit), so that only preexisting magnetic fluctuations of interstellar turbulence are present. In the second case, we enable PUI feedback, allowing self-generated waves to develop in addition to the large-scale turbulence. From a comparison between these two cases, we can identify the relative importance of turbulent mirroring and instability-driven waves in PUI pitch-angle evolution.

3.1. The Evolution of the Magnetic Fluctuations

Since small-scale fluctuations driven by PUIs are the crucial difference between the two cases, we first examine the power spectra of the magnetic fluctuations as a function of wavenumber k in the simulations. Figure 1 shows magnetic power spectra at $t\Omega_i = 0$ (black curves), 100 (blue curves), 1000 (green curves), and 3500 (red curves) in the cases without and with PUI feedback in panels (a) and (b), respectively. The initialized fluctuations have a Kolmogorov slope of $\gamma = -5/3$, resembling the Voyager observation (e.g., L. F. Burlaga et al. 2018).

In panel (a), without the PUI feedback, the spectra at $kd_i \lesssim 0.6$ remain essentially unchanged throughout the simulation. At higher wavenumbers, we find a noticeable attenuation of wave power, which is likely due to numerical dissipation. This attenuation begins immediately after the start of the simulation and shows little further evolution beyond $t\Omega_i = 1000$. The associated change in magnetic energy is negligible, with a relative decrease of $\lesssim 10^{-4}$ by $t\Omega_i = 3500$.

For panel (b), when the PUI feedback is included, we observe the power enhancement due to the excited waves. The spectrum at $t\Omega_i = 100$ (blue curve) exhibits an enhancement peaking around $kd_i \simeq 0.3$–0.4. As the particles gradually scatter toward smaller pitch angles and excite waves with longer wavelengths, the range of k with enhanced wave power becomes broader. This evolution can be reflected by the green curve ($t\Omega_i = 1000$) and the red curve ($t\Omega_i = 3500$) with enhancements peaked at $kd_i \simeq 0.2$ and 0.1, respectively.

In terms of magnitude, the peak power is about 1 order of magnitude larger than the initial (interstellar turbulence) level at the same k for $t\Omega_i = 100$, and increases to roughly 2 orders of magnitude larger for $t\Omega_i = 1000$ and 3500. Nevertheless, we have examined that the rms strength of $\delta B/B$ increases from $\sim$0.088 at $t\Omega_i = 0$ to $\sim$0.090 at $t\Omega_i = 3500$, indicating that the enhancement of wave amplitude due to ring-beam instabilities is still small compared with the initialized turbulent waves. It is worth noting that attenuation at $kd_i \gtrsim 1.0$ still exists. However, as the wavenumbers corresponding to the spectrum attenuation are greater than the typical self-excited waves with $kd_i \sim 0.05$–0.4, the scattering of the PUIs is likely not affected by the numerical dissipation.

For the ring-beam PUI distribution described in Section 2.2 as the mean parallel velocity $v_\parallel \sim V_{\rm A}$, the excited waves are mostly the AIC mode (e.g., V. Florinski et al. 2016). To confirm it, we have applied a Fourier-transform analysis and found that the dispersion relation of the excited waves lies along the Alfvén wave branch (not shown), consistent with expectations of excited waves for low frequency, i.e., $w < \Omega_i$.

The top panel of Figure 2 provides an overview of the perpendicular magnetic fluctuations, $\delta B_\perp$ for the two cases without (green curve) and with (red curve) PUI feedback as a function of X/D at $t\Omega_i = 3500$, where $D = 1000 d_i$ is the

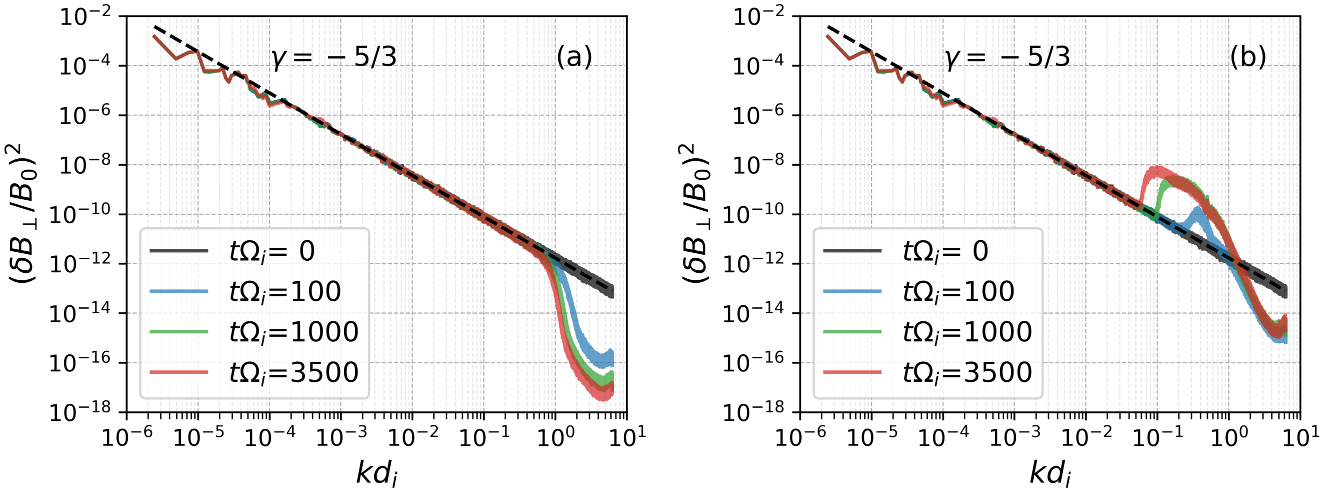

Figure 1. Power spectra of magnetic fluctuations at $t\Omega_i = 0$, 100, 1000, and 3500 are shown by the black, blue, green, and red curves, respectively. Panels (a) and (b) represent the cases without and with the feedback of PUIs, respectively. The black dashed lines indicate the spectra calculated using Equation (12), which has a Kolmogorov slope $\gamma = -5/3$.

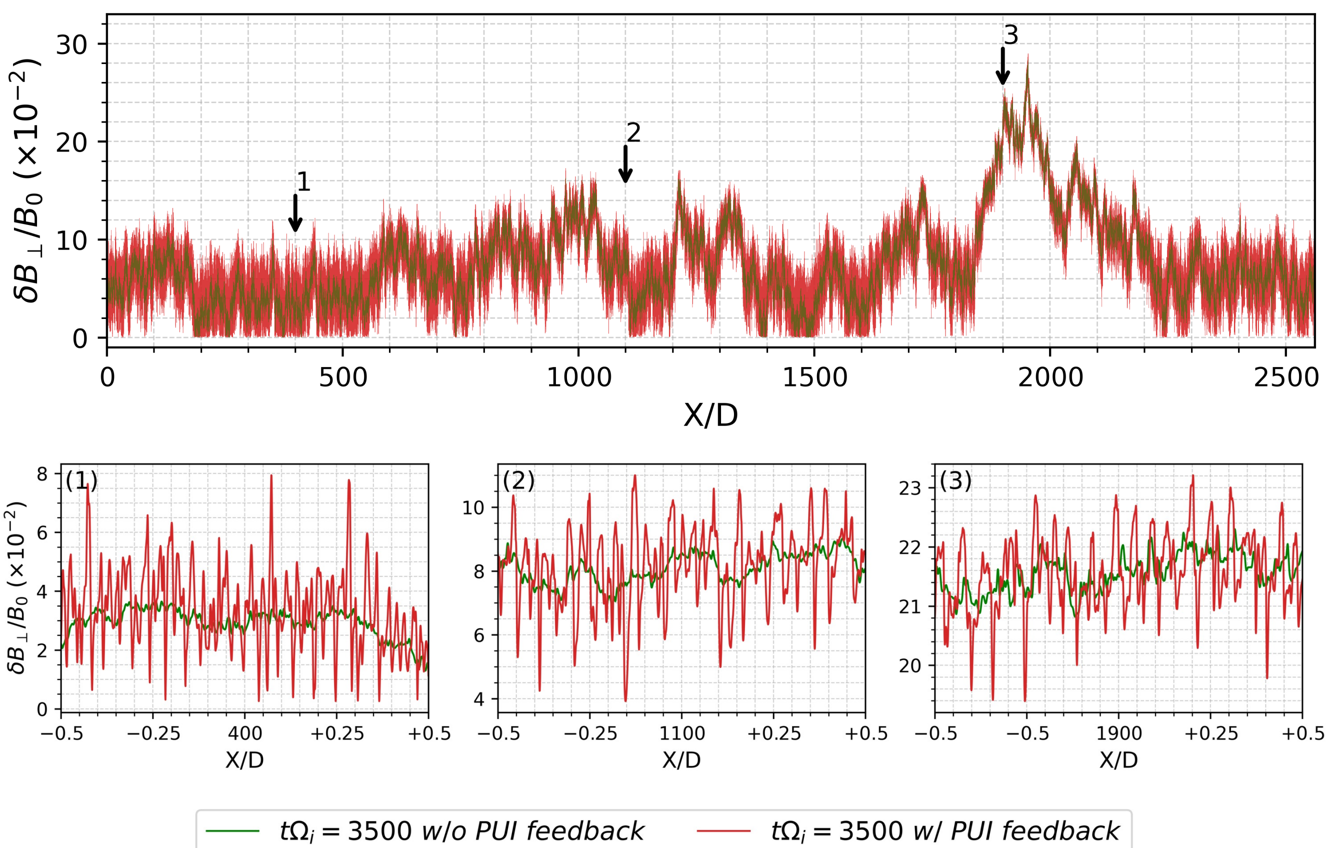

Figure 2. Magnetic fluctuations at $t\Omega_i = 3500$ for simulations without (green) and with (red) PUI feedback in the entire domain (top panel). The corresponding profiles at $X/D = 400$, 1100, and 1900 are presented in panels (1)–(3), respectively, where $D = 1000d_i$ is the scaling factor.

scaling factor. We can see that the fluctuation magnitude varies significantly across the box, reaching up to $\delta B_\perp/B_0 \sim 0.28$. Because the waves propagate at the Alfvén speed and cannot travel across a large fraction of the domain during the simulation time, the large-scale pattern of $\delta B_\perp$ remains nearly unchanged. The most important difference between the two curves is the excited waves, which cause additional fluctuations in the case with PUI feedback (red curve). To reveal the detailed difference between the two cases, we selected three local regions of width $1000d_i$ centered at $X/D = 400$ (panel (1)), 1100 (panel (2)), and 1900 (panel (3)), respectively. These locations are chosen because they represent different strengths of $\delta B_\perp$, which lead to distinct evolution of the PUI pitch-angle distributions, as we will

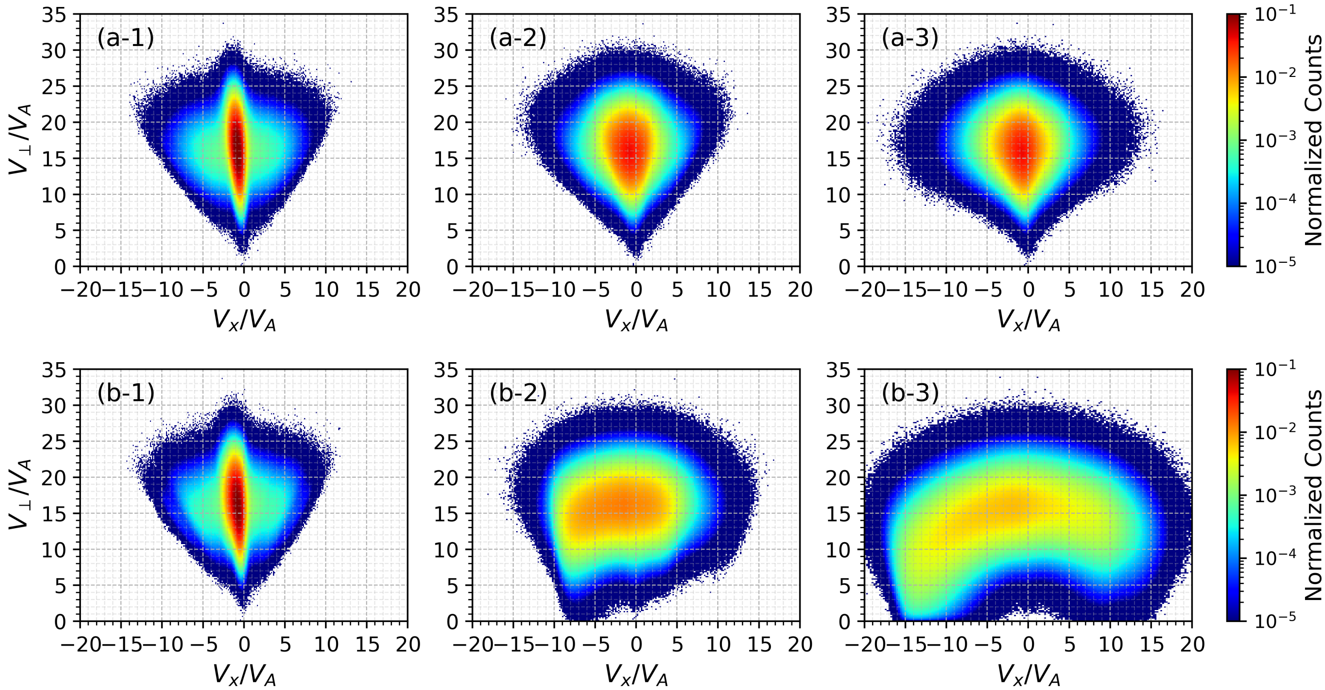

Figure 3. Velocity distributions in $V_\perp - V_x$ space. Panels in the top row ((a-1), (a-2), and (a-3)) and bottom row ((b-1), (b-2), and (b-3)) correspond to cases without and with PUI feedback, respectively. The three columns, from left to right, display the states at $t\Omega_i = 100$, 1000, and 3500. The color bar indicates the normalized particle phase density.

discuss in Section 3.3. The averaged amplitude of the excited waves is on the order of $\delta B_\perp / B_0 \sim 0.02$. From the panels (1), (2), and (3), we can read that their characteristic wavelength is $\sim$25 d_i, corresponding to a resonant wavenumber $kd_i \sim 0.25$. It is consistent with the scale of the enhanced power in Figure 1(b).

3.2. Evolution of Pitch-angle Distribution

Figure 3 shows the PUI velocity distributions for the cases without and with PUI feedback in the top and bottom rows, respectively. From left to right, the columns correspond to $t\Omega_i = 100$, 1000, and 3500, matching the times used in the power spectra of Figure 1. The initial distribution at $t\Omega_i = 0$ is not shown here, but it agrees well with the NSW velocity distribution described in J. Heerikhuisen et al. (2016). At $t\Omega_i = 100$, both runs exhibit some scattering away from the initial narrow structure of the red region. However, in the case with feedback (panel (b-1)), the densest part of the distribution (red and pink region) is slightly shifted more toward negative μ (μ is the pitch-angle cosine), indicating an early asymmetry in pitch-angle scattering. This behavior suggests enhanced pitch-angle scattering in the presence of self-generated waves compared to the case without feedback, and a persistent barrier to crossing $\mu = 0$ (e.g., J. R. Jokipii 1966; R. C. Tautz et al. 2008). At later times, $t\Omega_i = 1000$ and 3500, the two cases have significant differences. Without PUI feedback (panels (a-2) and (a-3)), the distribution remains strongly anisotropic, with the main high-density region largely preserved and confined to $V_x \approx -5V_A$ to $3V_A$. In contrast, when PUI feedback is included (panels (b-2) and (b-3)), pitch-angle diffusion becomes much more efficient, and the distribution spreads over a much wider range of velocities, approaching a nearly isotropic state.

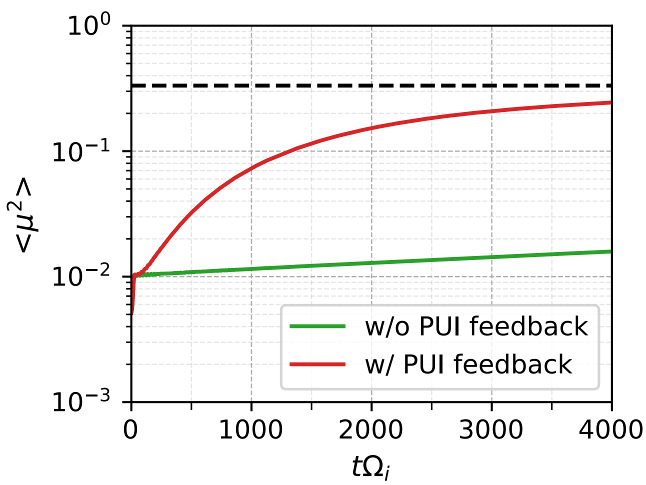

Figure 4. Evolution of $\langle \mu^2 \rangle$ for the cases without (green curve) and with (red curve) the PUI feedback in the simulation, respectively. The black dashed line represents the $\langle \mu^2 \rangle = 1/3$ for an isotropic distribution.

We use the averaged square of the pitch-angle cosine, $\langle \mu^2 \rangle$, as a measure of the anisotropy of the PUI pitch-angle distribution. Figure 4 shows the time evolution of $\langle \mu^2 \rangle$ for the cases without and with PUI feedback, plotted as the green and red curves, respectively. The black dashed line marks $\langle \mu^2 \rangle = 1/3$, corresponding to an isotropic distribution. Initially, $\langle \mu^2 \rangle \approx 0.005$ in both runs and increases rapidly to $\sim$0.01 within the first few tens of gyroperiods. This early, fast growth reflects a transient adjustment of the PUIs to the preexisting magnetic turbulence, during which the system relaxes toward a quasi-steady configuration. After this transient phase, in the case without PUI feedback (green curve), $\langle\mu^2\rangle$ increases approximately exponentially, appearing as a nearly linear trend on the logarithmic y-axis. Extrapolating this trend yields an isotropization timescale of $\sim 2.0 \times 10^5\,\Omega_i^{-1}$ for the distribution to reach $\langle\mu^2\rangle = 1/3$, which corresponds to a few months.

When PUI feedback is included (red curve), right after the initial transient adjustment, there is a time period (until $t\Omega_i \sim 100$) where $\langle\mu^2\rangle$ grows slowly, nearly identical to the green curve. The reason is that during this phase, the instability waves are yet to be excited, so that the particles are mainly scattered due to the background fluctuations. After that $\langle\mu^2\rangle$ grows much more rapidly up to $t\Omega_i \simeq 1000$ ($\sim$7.3 hr) and then continues to increase at later times. The corresponding isotropization time is on the order of one day, which is much shorter than the typical PUI lifetime of $\sim$1 yr. In particular, global simulations by Y. Huang et al. (2025) indicate that the most favorable pitch-angle range for producing an ENA ribbon with observed width and intensity is $\mu \sim -0.3$ to $\sim$0.3 (neglecting the draping of the local interstellar magnetic field), corresponding to $\langle\mu^2\rangle \sim 0.06$. Our results therefore show that, once self-generated waves from the secondary PUIs are taken into account, the PUIs could reach this level of anisotropy for producing an IBEX ribbon in several hours, well before they are typically neutralized again.

3.3. Spatial Variations of PUI Pitch-angle Diffusion within the Simulation Domain

In this section, we investigate the spatial distribution of $\langle\mu^2\rangle$ and compare in detail how turbulent mirroring alone and self-generated waves shape the PUI distributions. For the case without PUI feedback, Figure 5 shows the evolution of the spatial profile of $\langle\mu^2\rangle$ (panel (a)), the domain-averaged pitch-angle distribution (panel (a-0)), and the local pitch-angle distributions at $X/D = 400$ (panel (a-1)), 1100 (panel (a-2)), and 1900 (panel (a-3)). In each panel, we plot snapshots at $t\Omega_i =$ 0 (black dotted), 500 (blue solid), 1000 (green solid), 2000 (orange solid), and 3500 (red solid). The black dotted curves in panels (a-0)–(a-3) are scaled by a factor of 0.3 for clarity. Panel (a) shows that $\langle\mu^2\rangle$ is obviously nonuniform in space, indicating that the strength of turbulent mirroring varies across the domain. This is expected since the preexisting fluctuations have a correlation length on the same scale as L_x.

The domain-averaged pitch-angle distributions in panel (a-0) show that, without PUI feedback, the anisotropy is only slowly reduced by pitch-angle diffusion, consistent with the gradual increase of $\langle\mu^2\rangle$ in Figure 4. The maximum pitch-angle cosine allowed by turbulent mirroring is (e.g., T. G. Northrop & E. Teller 1960)

$$\mu_{\max} \simeq \sqrt{\frac{\delta B}{\delta B + B_0}}, \tag{15}$$

which depends on the local magnetic fluctuation strength. Note that in our problem, only perpendicular magnetic fluctuations are permitted. Using the domain-averaged variance $\delta B/B_0 \simeq 0.088$, we obtain $\mu_{\max} \simeq 0.28$, consistent with the bandwidth in panel (a-0). To illustrate the spatial variation, we examine three slices at $X/D = 400$ (panel (a-1)), 1100 (panel (a-2)), and 1900 (panel (a-3)). At $X/D = 400$, where $\delta B/B_0 \simeq 0.03$ (Figure 2), the distributions remain confined to a narrow band, in agreement with $\mu_{\max} \simeq 0.17$. At $X/D = 1100$ and 1900, where $\delta B/B_0 \simeq 0.081$ and 0.216, the corresponding $\mu_{\max} \simeq 0.27$ and 0.42 result in a wider quasi-trapped region, and the PUIs quickly fill this range with only gradual evolution thereafter. Overall, Figure 5 shows that turbulent mirroring produces spatially varying confinement in μ that is consistent with the mirroring process.

The situation is markedly different when PUI feedback and self-generated waves are included (Figure 6). Compared with the case without feedback, the spatial distribution of $\langle\mu^2\rangle$ (panel (b)) becomes progressively less anisotropic as time advances, and by $t\Omega_i = 3500$ the red curve has approached $\langle\mu^2\rangle \simeq 0.3$ over most of the domain. This corresponds to a nearly isotropic pitch-angle distribution on the global scale. The domain-averaged distributions in panel (b-0) show that the initially narrow, highly anisotropic peak gradually flattens out, while the strong peak has essentially disappeared at $t\Omega_i = 3500$. These features indicate that self-generated waves dominate pitch-angle diffusion and can overcome the constraints imposed by turbulent mirroring.

Panels (b-1)–(b-3) show local pitch-angle distributions at $X/D = 400$, 1100, and 1900, i.e., at positions that previously exhibited different mirroring strengths in Figure 5. Although the overall rms of the magnetic fluctuations does not change substantially relative to the case without feedback, the evolution of the pitch-angle distributions is fundamentally altered. In all three local regions, we now see strong pitch-angle scattering that quickly fills the previously quasi-trapped μ regions and drives the distributions toward isotropy. The differences between the slices are most apparent at $t\Omega_i = 500$, when the self-generated waves are still growing. For example, in panel (b-1), the blue and green curves appear as smooth broadening of the initial distribution, while in panels (b-2) and (b-3), the blue curves still show pronounced peaks near the edges of the mirroring range, reflecting the residual influence of turbulent mirroring where $\delta B/B_0$ is larger. After $t\Omega_i = 500$, however, the self-generated waves become strong enough at the resonant scales that they dominate scattering, allowing PUIs to escape from the quasi-trapped μ region and thereby erasing the mirroring-induced structures seen in the case without feedback.

These results show that self-generated waves can efficiently scatter PUIs even when their contribution to the total rms magnetic fluctuation is very small. The mirroring bound (Equation (15)), which could describe the case without feedback, breaks down once PUI-driven instability grows. In other words, PUI pitch-angle diffusion is controlled not simply by the overall fluctuation level, but especially by the self-excited wave power at resonant scales. Therefore, in the case with PUI feedback, the enhanced self-excited waves fundamentally change the pitch-angle diffusion and enables rapid isotropization of the PUIs even in the presence of large-scale fluctuations.

4. Summary and Discussion

In this work, we have investigated the stability of a PUI ring-beam population embedded in large-scale interstellar turbulence and microscale self-generated waves, using the MHD–PIC module of ATHENA++. In this approach, the PUIs are treated as macroparticles, and their feedback on the background plasma is self-consistently included. The PUIs are initialized from a NSW parent distribution based on global heliosphere modeling, while the interstellar magnetic fluctuations are represented by a slab spectrum of parallel-

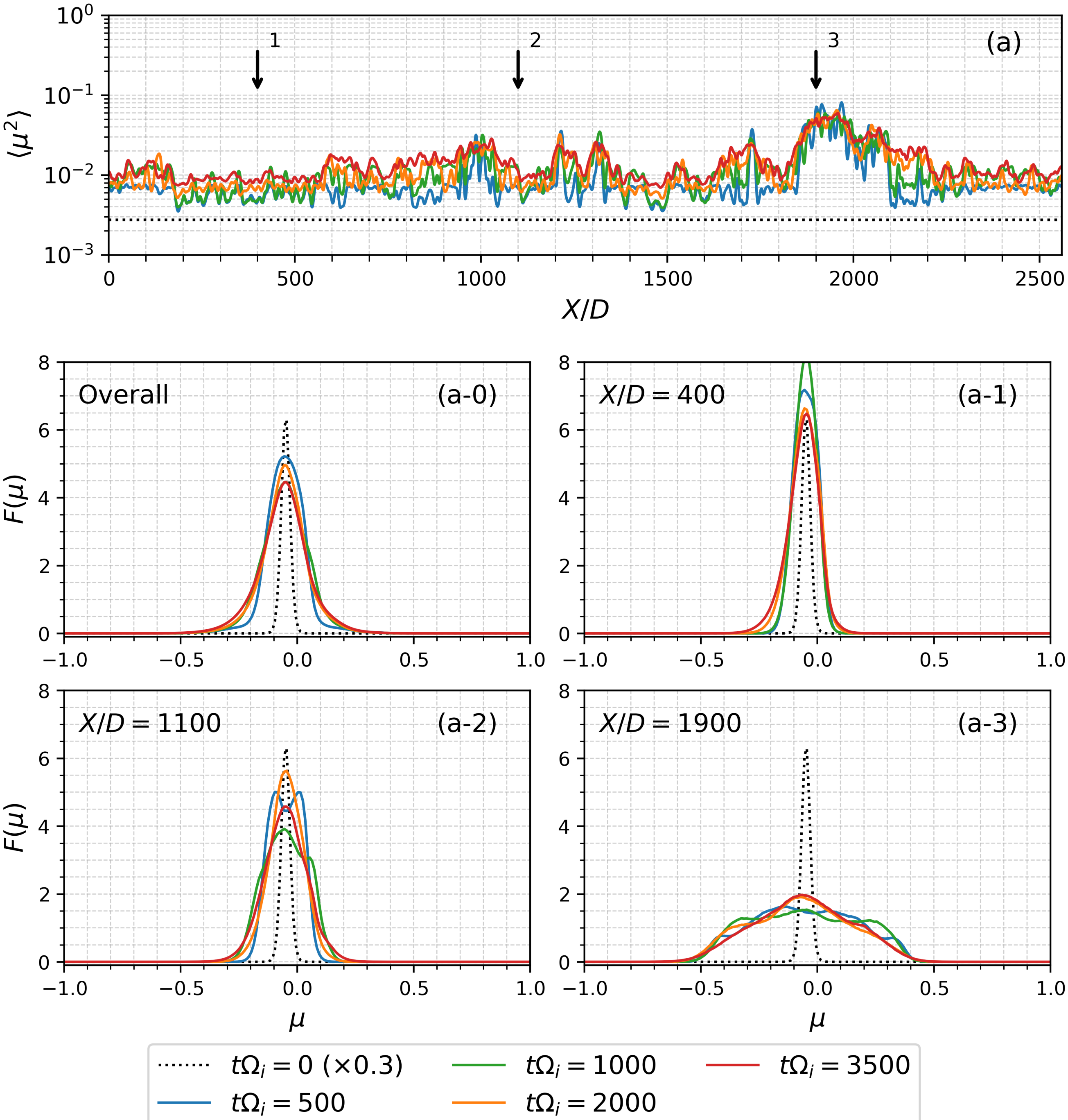

Figure 5. Evolution of the spatial distribution of $\langle \mu^2 \rangle$ (panel (a)), domain-averaged pitch-angle distribution (panel (a-0)), and pitch-angle distributions at $X/D = 400$ (panel (a-1)), 1100 (panel (a-2)), and 1900 (panel (a-3)) for the case without PUI feedback. Here, $D = 1000d_i$ is the scaling factor. In each panel, snapshots at $t\Omega_i = 0$ (black dotted), 500 (blue solid), 1000 (green solid), 2000 (orange solid), and 3000 (red solid) are shown. Note that in panels (a-0)–(a-3), the black dotted curves are scaled by a factor of 0.3 for clarity.

propagating Alfvén waves with a Kolmogorov power law, consistent with Voyager observations.

We find that the ring-beam distribution excites low-frequency waves near the AIC branch. The power spectra show clear enhancements of typical self-excited waves peaked around $kd_i \sim 0.1$–0.4, with peak power exceeding the background turbulence level by up to 2 orders of magnitude. These self-generated waves fundamentally change the PUI pitch-angle evolution: the PUI distribution is rapidly scattered toward isotropy, and the domain-averaged $\langle \mu^2 \rangle$ reaches ∼one-third on the order of one day, far shorter than the typical PUI lifetime of ∼1 yr. Our results indicate that the resonant scattering could overwhelm large-scale turbulent mirroring in PUI pitch-angle diffusion.

These results have important implications for IBEX ribbon models that rely on long-lived anisotropic PUI distributions beyond the heliopause. While earlier test-particle simulations in prescribed turbulence (e.g., J. Giacalone & J. R. Jokipii 2015;

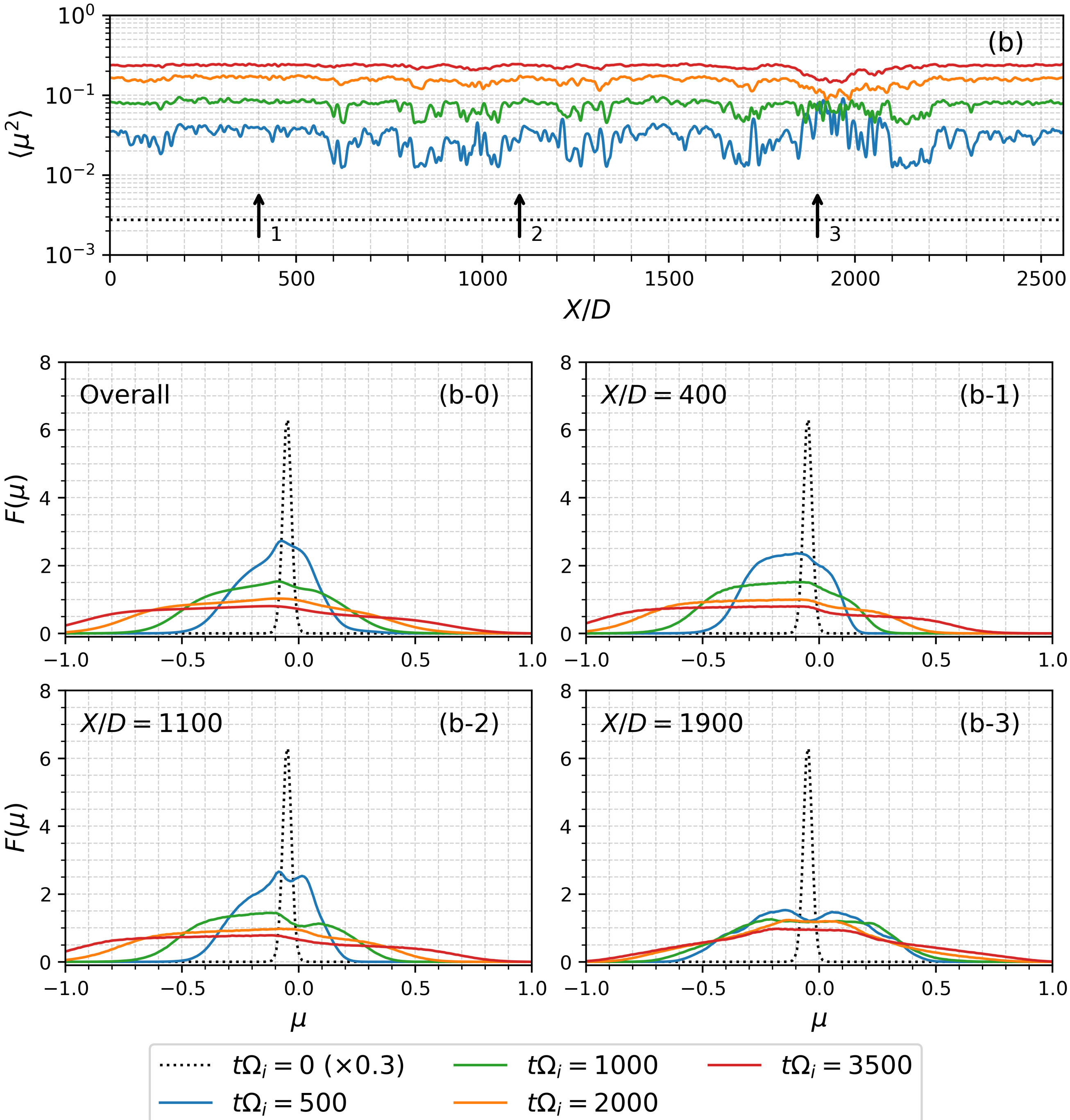

Figure 6. The same as Figure 5, but for the case with PUI feedback.

E. J. Zirnstein et al. 2020) showed that large-scale mirroring can trap PUIs near $\mu \approx 0$ and produce strongly anisotropic distributions in the ribbon source region, our self-consistent MHD–PIC calculations support earlier theoretical arguments (e.g., V. Florinski et al. 2010) that such ring-beam distributions are intrinsically unstable: self-generated waves rapidly scatter the PUIs toward isotropy on timescales much shorter than their lifetime, allowing them to escape from magnetic traps. This represents a fundamental challenge to turbulent-mirroring ribbon scenarios.

Our study is subject to a few simplifying assumptions. We adopted a 1D slab model of turbulence with parallel-propagating Alfvén waves and used a typical set of background parameters at a selected location beyond the heliopause. Another simplification concerns the wave physics: we use the ideal-MHD Ohm's law and neglect dispersive/kinetic corrections (e.g., Hall and electron-pressure terms), which become important near ion scales and modify the dispersion and polarization of Alfvénic fluctuations (including the AIC/ion-cyclotron branch). In addition, electrons are not treated kinetically in our MHD–PIC setup; they enter only through the fluid closure, which can also influence the wave properties at small scales.

Another limitation of the present analysis is that the source term in the simulations is prescribed entirely at initialization, and therefore does not capture the gradual ionization of neutral SW particles. The continuous injection of the ionized particles may delay the onset of rapid scattering to later times (K. Liu et al. 2012). For this reason, the role of continuous injection is worth investigating because it may qualitatively change the parameter regime and conditions under which wave growth and pitch-angle scattering become effective.

In future work, the same MHD–PIC framework can be extended to higher dimensions with more realistic turbulence geometries and PUI injection, and a broader range of parameters such as the large-scale fluctuation strength. Such studies will be crucial for assessing whether any viable configuration can sustain the degree of PUI anisotropy required to reproduce the observed IBEX ribbon, or whether alternative mechanisms must be invoked.

Acknowledgments

This work at Los Alamos National Laboratory is supported by the Laboratory Directed Research and Development program under project No. 20220107DR. X.S. acknowledges support by Multimessenger Plasma Physics Center (MPPC, NSF grant PHY2206607). E.J.Z. acknowledges support from NASA's IBEX mission (80NSSC20K0719).

ORCID iDs

Yifan Huang https://orcid.org/0000-0002-0422-2925
Xiaochen Sun https://orcid.org/0009-0009-7676-6188
Sung Jun Noh https://orcid.org/0000-0002-8032-7833
Eric J. Zirnstein https://orcid.org/0000-0001-7240-0618
Daniel B. Reisenfeld https://orcid.org/0000-0003-1874-9450
Hui Li https://orcid.org/0000-0003-3556-6568
Vladimir Florinski https://orcid.org/0000-0001-5485-2872
Jacob Heerikhuisen https://orcid.org/0000-0001-7867-3633

References

Bai, X.-N., Caprioli, D., Sironi, L., & Spitkovsky, A. 2015, ApJ, 809, 55
Bai, X.-N., Ostriker, E. C., Plotnikov, I., & Stone, J. M. 2019, ApJ, 876, 60
Boris, J., Shanny, R., & Laboratory, R. 1971, in Naval Research Laboratory Proc.: Fourth Conf. on Numerical Simulation of Plasmas, 1970, https://apps.dtic.mil/sti/citations/ADA023511
Burlaga, L. F., Florinski, V., & Ness, N. F. 2018, ApJ, 854, 20
Burlaga, L. F., Ness, N. F., & Stone, E. C. 2015, Sci, 341, 147
Florinski, V., Heerikhuisen, J., Niemiec, J., & Ernst, A. 2016, ApJ, 826, 197
Florinski, V., Zank, G. P., Heerikhuisen, J., Hu, Q., & Khazanov, I. 2010, ApJ, 719, 1097
Funsten, H. O., Allegrini, F., Bochsler, P., et al. 2009a, SSRv, 146, 75
Funsten, H. O., Allegrini, F., Crew, G. B., et al. 2009b, Sci, 326, 964
Fuselier, S. A., Allegrini, F., Funsten, H. O., et al. 2009, Sci, 326, 962
Gamayunov, K. V., Heerikhuisen, J., & Rassoul, H. 2017, ApJ, 845, 63
Gamayunov, K. V., Heerikhuisen, J., & Rassoul, H. K. 2019, ApJL, 876, L21
Giacalone, J., & Jokipii, J. R. 1999, ApJ, 520, 204
Giacalone, J., & Jokipii, J. R. 2015, ApJL, 812, L9
Heerikhuisen, J., Gamayunov, K. V., Zirnstein, E. J., & Pogorelov, N. V. 2016, ApJ, 831, 137
Heerikhuisen, J., Pogorelov, N. V., Zank, G. P., et al. 2010, ApJL, 708, L126
Huang, Y., Guo, F., Zirnstein, E. J., et al. 2025, ApJ, 987, 192
Isenberg, P. A. 2014, ApJ, 787, 76
Jokipii, J. R. 1966, ApJ, 146, 480
Liu, K., Möbius, E., Gary, S. P., & Winske, D. 2012, JGRA, 117, A10102
McComas, D. J., Lewis, W. S., & Schwadron, N. A. 2014, RvGeo, 52, 118
McComas, D. J., Allegrini, F., Bochsler, P., et al. 2009a, SSRv, 146, 11
McComas, D. J., Allegrini, F., Bochsler, P., et al. 2009b, Sci, 326, 959
McComas, D. J., Bzowski, M., Frisch, P., et al. 2010, JGRA, 115, A09113
Min, K., & Liu, K. 2018, ApJ, 852, 39
Mousavi, A., Liu, K., & Min, K. 2020, ApJ, 901, 167
Mousavi, A., Liu, K., & Sadeghzadeh, S. 2022, ApJ, 940, 37
Mousavi, A., Roytershteyn, V., Fraternale, F., & Pogorelov, N. 2025, ApJ, 980, 95
Niemiec, J., Florinski, V., Heerikhuisen, J., & Nishikawa, K. I. 2016, ApJ, 826, 198
Noh, S. J., Reisenfeld, D. B., Beesley, L. J., et al. 2025, ApJ, 980, 8
Northrop, T. G., & Teller, E. 1960, PhRv, 117, 215
Pogorelov, N. V., Heerikhuisen, J., Mitchell, J. J., Cairns, I. H., & Zank, G. P. 2009, ApJL, 695, L31
Reisenfeld, D. B., Allegrini, F., Christian, E. R., et al. 2026, SSRv, 222, 7
Roytershteyn, V., Pogorelov, N. V., & Heerikhuisen, J. 2019, ApJ, 881, 65
Schlickeiser, R. 2002, Cosmic Ray Astrophysics (Springer)
Schwadron, N. A., & McComas, D. J. 2013, ApJ, 764, 92
Schwadron, N. A., Bzowski, M., Crew, G. B., et al. 2009, Sci, 326, 966
Stone, J. M., & Gardiner, T. 2009, NewA, 14, 139
Stone, J. M., Tomida, K., White, C. J., & Felker, K. G. 2020, ApJS, 249, 4
Summerlin, E. J., Viñas, A. F., Moore, T. E., Christian, E. R., & Cooper, J. F. 2014, ApJ, 793, 93
Sun, X., & Bai, X.-N. 2023, MNRAS, 523, 3328
Tautz, R. C., Shalchi, A., & Schlickeiser, R. 2008, ApJ, 672, 642
van Leer, B. 1979, JCoPh, 32, 101
Xu, S., & Li, H. 2023, ApJ, 957, 97
Zank, G. P., Nakanotani, M., & Webb, G. M. 2019, ApJ, 887, 116
Zirnstein, E. J., Giacalone, J., Kumar, R., et al. 2020, ApJ, 888, 29
Zirnstein, E. J., Heerikhuisen, J., & Dayeh, M. A. 2018, ApJ, 855, 30
Zirnstein, E. J., Heerikhuisen, J., Funsten, H. O., et al. 2016, ApJL, 818, L18
Zirnstein, E. J., McComas, D. J., Giacalone, J., et al. 2025, ApJ, 993, 219
Zirnstein, E. J., McComas, D. J., Schwadron, N. A., et al. 2019, ApJ, 876, 92